Photo-Electrochemical Conversion of CO_2 Under Concentrated Sunlight Enables Combination of High Reaction Rate and Efficiency

Etienne Boutin, Mahendra Patel, Egon Kecsenovity, Silvan Suter, Csaba Janáky, and Sophia Haussener*

Photo-electrochemical production of solar fuels from carbon dioxide, water, and sunlight is an appealing approach. Nevertheless, it remains challenging to scale despite encouraging demonstrations at low power input. Higher current densities require notable voltage input as ohmic losses and activation overpotentials become more significant, resulting in lower solar-to-CO conversion efficiencies. A concentrated photovoltaic cell is integrated into a custom-made heat managed photo-electrochemical device. The heat is transferred from the photovoltaic module to the zero-gap electrolyzer cell by the stream of anodic reactant and produce synergetic effects on both sides. With solar concentrations up to 450 suns (i.e., 450 kW m^{-2}) applied for the first time to photo-electrochemical reduction of CO_2, a partial current for CO production of 4 A is achieved. At optimal conditions, the solar-to-CO conversion efficiency reaches 17% while maintaining a current density of 150 mA cm^{-2} in the electrolyzer and a CO selectivity above 90%, representing an overall 19% solar-to-fuel conversion efficiency. This study represents a first demonstration of photo-electrochemical CO_2 reduction under highly concentrated light, paving the way for resource efficient solar fuel production at high power input.

1. Introduction

Photoelectrochemical (PEC) reduction of CO_2 aims at using CO_2 from a point source or from an appropriated atmospheric or oceanic capture process to transform it into valuable molecules (fuel or chemicals such as carbon monoxide (CO), methanol, methane, ethanol, ethylene, etc.) with solar energy.[1–3] It complements the efforts currently undertaken to reduce CO_2 anthropogenic emissions and offers a long-term storage for solar energy while opening the way toward a post-fossil fuels chemical industry. Over the recent years, traditional PEC (with direct semiconductor-liquid electrolyte interfaces) have been less common and instead integrated devices directly coupling a photovoltaic (PV) cell (or a buried junction) with an electrochemical (EC) cell have been investigated with encouraging solar-to-fuel energy conversion efficiencies (up to 20%).[4] Separate optimization of charge separation and collection (PV) and catalysis (EC) is possible in such a system since effects are spatially decoupled. For this reason, they could more logically be referred to as photo-electrochemical (P-EC). The same definition applies to recent reports of photo-cathode or photo-anode in contact with the electrolyte but featuring a buried PV junction.[5–7] In the majority of P-EC reports, CO was the targeted product through Equation 1 resulting from Equation 1a,b half-cell reactions, with the EC part being either a H-cell,[8–16] a one compartment cell (no separator),[17,18] a two compartments flow cell (membrane separator),[4,19–24] a monolithic P-EC cell,[25–27] a proton exchange membrane based (PEM) zero gap cell,[28] or an anion exchange membrane based (AEM) zero-gap stack.[29] All these studies were performed at irradiation intensity of 1 sun (1 kW m^{-2}, see Discussion S1 (Supporting Information) for detailed definition)[4,8–16,18,19,21–29] or below[17,20] at the exception of one report at 3.25 suns.[19] All these experiments are summarized in Table S1 (Supporting Information).

$$CO_{2(g)} \leftrightarrow CO_{(g)} + 1/2O_{2(g)} \qquad \frac{\Delta_r G^0}{2F} = 1.33\,V \qquad (1)$$

$$CO_{2(g)} + 2e^- + 2H^+ \leftrightarrow CO_{(g)} + H_2O_{(l)} \qquad E^0 = -0.1\,V\ vs.\ RHE \qquad (1a)$$

$$H_2O_{(l)} \leftrightarrow 1/2O_{2(g)} + 2e^- + 2H^+ \qquad E^0 = 1.23\,V\ vs.\ RHE \qquad (1b)$$

A few reports targeted formate[30–37] or hydrocarbons[38–43] with solar-to-chemical energy conversion efficiencies below or
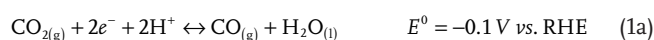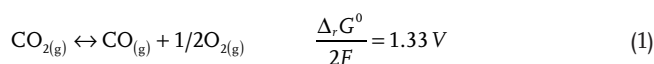
E. Boutin, M. Patel, S. Suter, S. Haussener
Laboratory of Renewable Energy Science
and Engineering EPFL
Station 9, Lausanne 1015, Switzerland
E-mail: sophia.haussener@epfl.ch
E. Kecsenovity, C. Janáky
Department of Physical Chemistry and Materials Science
Interdisciplinary Excellence Centre
University of Szeged
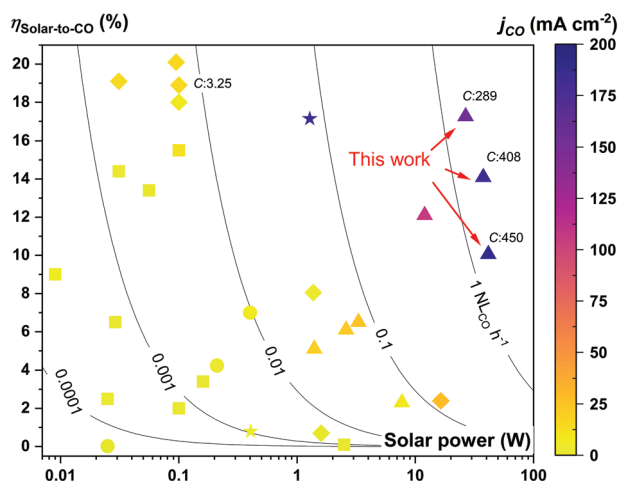Aradi Square 1, Szeged H-6720, Hungary

Figure 1. Solar-to-CO conversion efficiency and CO partial current density in the electrolyzer as a function of incoming solar power for previously reported light-driven P-EC reduction of CO_2 into CO experiments.[4,8–29] Solar concentration ≥ 1 sun. Electrolyzer part: H-cell (square), flow cell (diamond), monolithic stack (circle), zero-gap (triangle) and no membrane cell (star). More details and references available in Table S1 (Supporting Information). Isolines represent CO production rates in normal liter per hour (NL h^{-1}). For demonstrations with concentrated solar irradiation, the number of suns is displayed. The data reported in the present study are highlighted with red arrows.

equal to 10%. The higher interest for CO originates from its broad use in chemical industry along with the possibility to drive the reaction selectively, which is rarely reported for hydrocarbon formation.[44] **Figure 1** gathers previous reports of P-EC CO_2 reduction into CO at 1 sun and above. Some experiments are yielding interesting solar-to-CO conversion efficiencies (above 10%) and some are made at solar input powers above the typical 0.1 W experiment (i.e., 1 sun irradiation on 1 cm^2 photoabsorber). But only two demonstrations have met the two conditions, high efficiency and large input powers, simultaneously. One involved 120 cm^2 silicon solar cells connected to a separate EC with a Ag dendrite catalyst at the cathode.[29] They used a zero-gap configuration with an AEM, for the first time in P-EC CO_2 reduction, to limit voltage losses. It allowed to reach 12% solar-to-CO conversion efficiency, at 1.2 W solar input and up to 105 mA cm^{-2} partial current density for CO in the electrolyzer. The other study involves a choline/chloride electrolyte in a one compartment flow cell reactor.[17] They reported solar-to-CO efficiencies of 18 and even 23% while the CO partial current density (j_{CO}) was 182 and 86 mA cm^{-2} at 1 and 0.5 suns respectively. The absence of a separator along with the large current at near zero overpotential, however, casts doubt on the nature of the reaction reported. These two reports are also the only ones to exceed 50 mA cm^{-2} in the electrolyzer. Furthermore, there are only two reports above 10 W solar input power,[22,29] and the maximum solar concentration investigated is 3.25 suns.[19] The challenge to yield a high solar-to-CO conversion efficiency at high solar power input is related to the increase of voltage losses. The solar-to-CO conversion efficiency is usually calculated as in Equation 2a (for Equation 1 as the overall equation) and can be reshuffled into Equation 2b to break it down into four elemental terms: the efficiency of the PV (η_{PV}), that relates

the electrical power of the PV delivered at its maximal power point ($P_{mp} = U_{PV,mp}I_{PV,mp}$) with the incoming solar power, the matching efficiency between the PV and EC (η_{op}) that relates the actual operating power with the optimal power, the current efficiency of the EC part ($\eta_{EC,current}$ usually referred to as Faradaic efficiency, FE_{CO}), and the voltage efficiency of the P-EC cell ($\eta_{P-EC,voltage}$) that relates thermodynamic energy of the reaction per electron with the provided power per electron.

$$\eta_{Solar-to-CO} = \frac{I_{CO}\left(E^0_{O_2/H_2O} - E^0_{CO_2/CO}\right)}{P_{Solar}} \tag{2a}$$

$$\eta_{Solar-to-CO} = \underbrace{\frac{U_{PV,mp}\,I_{PV,mp}}{P_{Solar}}}_{\eta_{PV}} \underbrace{\frac{U_{PV}\,I_{Total}}{U_{PV,mp}\,I_{PV,mp}}}_{\eta_{op}} \underbrace{\frac{I_{CO}}{I_{Total}}}_{\eta_{EC,current}} \underbrace{\frac{\left(E^0_{O_2/H_2O} - E^0_{CO_2/CO}\right)}{U_{PV}}}_{\eta_{P-EC,voltage}} \tag{2b}$$

State-of-the-art η_{PV} have now been reported above 40%, even for commercial cells.[45,46] Near 100% η_{op} is reachable by simply adapting the PV to EC surface ratio.[9,11] Near 100% $\eta_{EC,current}$ (FE_{CO}) are also often reported for various catalysts.[47] The last term, $\eta_{P-EC,voltage}$, can also be optimized to near 100% by connecting in series the appropriate number of electrolyzers and PV cells.[48,49] Overall, a solar-to-CO conversion efficiency of near 40% could theoretically be achieved, following the above mentioned strategies. Nevertheless, the optimization of $\eta_{P-EC,voltage}$ would make the current densities in the electrolyzer part smaller and smaller (approaching zero) as the total overpotential is decreased and following adjustment of η_{op} would result in a large EC surface area, making any upscaling extremely material-intensive. As a consequence, the necessary increase in current densities and the resulting increase in overpotentials and ohmic resistivity are responsible for the observed trade-off between incoming solar power (i.e., power density of the device) and solar-to-CO conversion efficiency. New strategies are required to effectively reduce the surfaces of both the PV and EC units, at high power input, without significant losses in solar-to-CO conversion efficiency.[50]

We have reported recently that using concentrated sunlight can be a viable option to industrialized solar driven CO_2 conversion.[51] In this study, a GaInP/GaInAs/Ge triple junction concentrated photovoltaic (CPV) cell that displays enhanced voltage output at high concentration was used. The latter is integrated into a heat managed P-EC cell where the EC part is a zero-gap electrolyzer.[52,53] This configuration reduces the ohmic losses in the cell thanks to a 15 µm thick solid electrolyte between the anode and cathode. A previously reported method of activation is applied to reduce cathodic overpotential and increase membrane conductivity.[53] The activation overpotential, at both the cathode and anode, can be further decreased at elevated temperature, which is made possible by the anodic stream that simultaneously acts as a heat management fluid, cooling the CPV part while warming the EC part.[54] With all these features combined, we report for the first time a P-EC CO_2 conversion into CO with up to 41.4 W solar input power, using only 0.92 cm^2 CPV part and 25 cm^2 EC part. At 289 suns, current densities in the CPV and EC parts reach 4.1 and 0.15 A cm^{-2} respectively, while reaching a solar-to-CO conversion efficiency of 17% (Figure 1). The combination of high input power together with high solar-to-CO conversion efficiency
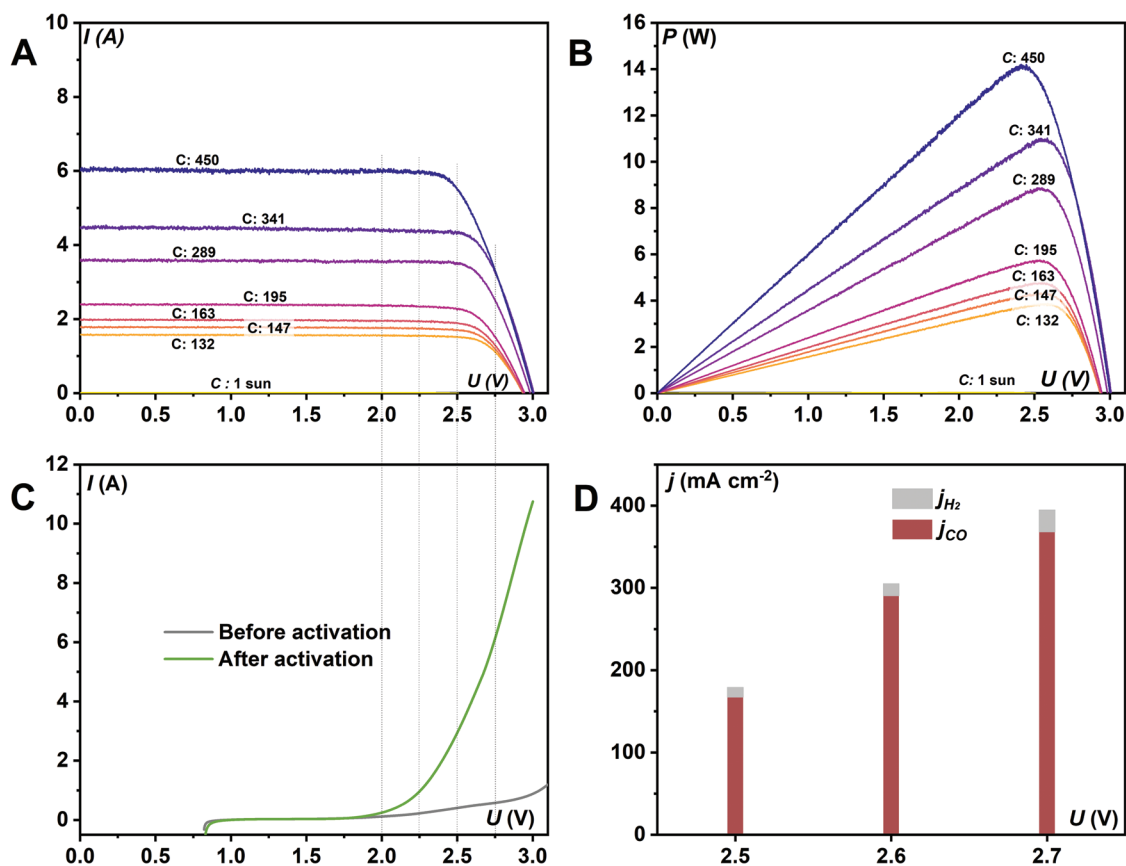
Figure 2. Independent characterization of CPV and EC parts before integration. A) I–U curves on the CPV module at various solar concentrations. B) Electrical power from the same CPV module as a function of voltage at various concentrations. C) LSV on EC cell before and after activation with 10 cm^3 of 1 M CsOH solution in 1:3 isopropanol/water mixture. D) CO and H$_2$ partial current density in the EC part (from GC analysis) 5 min after performing the cathode activation, recorded at different cell voltages. A) and B) estimated T_{CPV} are between 45 and 52 °C and S_{CPV}: 0.92 cm^2. (C) and (D) are performed on EC part with 60 °C ultrapure water at the anode, 312 sccm CO$_2$ at the cathode and S_{EC}: 25 cm^2.

results in the first report to date of P-EC CO$_2$ reduction into CO at a production rate surpassing 1 NL h^{-1}.

To be integrated together in a heat managed P-EC device, the EC and PV parts must follow a set of requirements. The PV part should have a high η_{PV} efficiency while providing enough current and voltage to the EC part so that both work at high current density. The CPV cell employed in this study is a commercial triple-junction (GaInP/GaInAs/Ge) cell protected with black epoxy resin with an exposed surface of 0.92 cm^2. The CPV cell is cooled by a stream of ultrapure water that flows between the top of the CPV cell and a quartz window. This integrated cooling approach is important to maintain a large voltage output of the CPV cell as its U_{oc} decreases with increasing temperature (see Discussion S2 (Supporting Information) for quantitative assessment of CPV temperature). When cooled by a stream of ultrapure water, the estimated CPV temperature reaches values between 45 and 52 °C. In these conditions the open circuit voltage (U_{oc}) reaches ≈3V for concentrations (C) above 250 suns (**Figure 2**A) and a U_{mp} superior to 2.4 V even at high current densities (Figures 2B; Figure S1, Supporting Information). In this range of concentration, the current provided by a ≈1 cm^2 CPV cell is 5 A and above. This high current requires that any electrical contact inside the device is free of parasitic

series resistance. As an illustration, even a 20 mΩ series resistance would results in 100 mV drop, accompanied with strong penalties to the EC performance. The EC part should provide high selectivity and high current density for CO$_2$ splitting into CO and O$_2$ (Equation 1) with voltages in the [2.4–2.8V] range. Additionally, the reactant at the anode side, which is also the coolant of the CPV module, can only be ultrapure water for two reasons. First, the cooling stream should be nonconductive to avoid a shortcut as it is in contact with both the CPV negative side when cooling it and the EC anode when it is oxidized. Furthermore, using an alkaline electrolyte solution would be detrimental for the stability of the CPV cell. Ultrapure water-based operation, however, is far from being trivial, as the presence of alkali metal cations at the cathode are necessary for high performance operation.[55] In our previous proof-of-concept study,[53] we have demonstrated a scalable ultrapure water-fed CO$_2$ electrolyzer cells operation, where the CO$_2$ reduction rates matched those measured when using alkaline electrolytes. To reduce ohmic losses, a zero-gap configuration is used, where a 15 μm thick AEM, acting as the solid electrolyte, replaces the liquid electrolyte used in other configurations.[52] The cathode is a gas diffusion electrode (GDE) made from a mixture of Ag nanoparticles (NPs) and Sustainion ionomer spray-coated

on carbon paper. The anode is made from a mixture of IrO_x NPs and Sustainion ionomer spray-coated on a Ti frit.

Since ultrapure water is provided at the anode, we have previously developed an operando activation method to provide the necessary alkali cations to the cathode. Using this method, the cathode of the electrolyzer cell is infused periodically with alkali cation-containing solutions. This solution has been optimized to have proper wetting properties, namely 10 cm^3 of 1 M CsOH solution in 1:3 isopropanol/water mixture.[53] In this process, the experimental set-up allows for the injection of this activation solution into the CO_2 feed, which is, in turn, pushed through the cathode GDE by the gas stream. When the activation solution is in the cell, the infused ions can adsorb on the catalyst surface. Such a strategy allowed to produce CO partial current densities above 200 mA cm^{-2} at cell voltages below 2.8 V. We analyzed the electrochemical behavior of the EC part in the voltage range of 2.5–2.7 V, where the maximum power output of the CPV module was expected. Linear sweep voltammetry (LSV) curves were recorded before and after activating the cathode GDE at 2.7 V (Figure 2C). The effect of activation is apparent from the approximately tenfold increased current densities, observed on the LSV traces as well as from the decrease of the cell impedance (Figure S2D, Supporting Information). Constant voltage electrolysis was carried out at U = 2.5, 2.6, and 2.7 V, starting with an aqueous anodic stream. After 200 s, activation mixture was injected to the cathode GDE side (Figures S2A–C, Supporting Information). Resulting currents were in the range of 2 to 10 A in this potential window with a current slowly decaying but completely recoverable through periodic reactivation of the material (after 45 min in Figure S2B, Supporting Information). The current decaying pace is a function

of various parameters that are addressed with Figure S2 (Supporting Information). An important advantage of this specific EC setup is its strong temperature dependence. As already reported, j_{CO} at a fixed applied voltage of 3.1 V is doubled or even tripled, (going from 75 to 150 or to 225 mA cm^{-2}) when the temperature of the stack is increased from 30° to 40° or to 60 °C respectively,[53] while j_{H2} remains limited to the range of [10–20] mA cm^{-2}. This not only results from enhanced electrode kinetics but also lower series resistance, as demonstrated by electrochemical impedance spectroscopy (EIS) of the EC cell[53] or the anionic membranes.[52] This significant temperature dependence along with matching current and voltage ranges make the PV and EC parts well suited for an integration into a heat managed device. To be noted in Figure 2, EC and PV traces cannot be directly superimposed as the real operating point position in the integrated device depends on the actual temperature of each part (a result of the coupled thermal transport and management), which are challenging to measure when the full P-EC cell is operated under concentrated illumination. Nevertheless, it appears that optimal current density and solar-to-CO conversion efficiency can be expected in the concentration range of [200–450] suns. To provide more information on the thermal aspect, several probes have been placed on the setup as described in Experimental section.

All P-EC experiments presented in this paper were performed with EPFL's High Flux Solar Simulator (HFSS)[56] with a custom-designed P-EC cell, made of three parts: the illuminated CPV part (**Figure 3**A), the zero-gap CO_2 electrolyzer cell (Figure 3B), and an adapter element that connects the two former parts (Figure 3C). The temperature of the ultrapure water anode stream is monitored at the inlet and outlet of
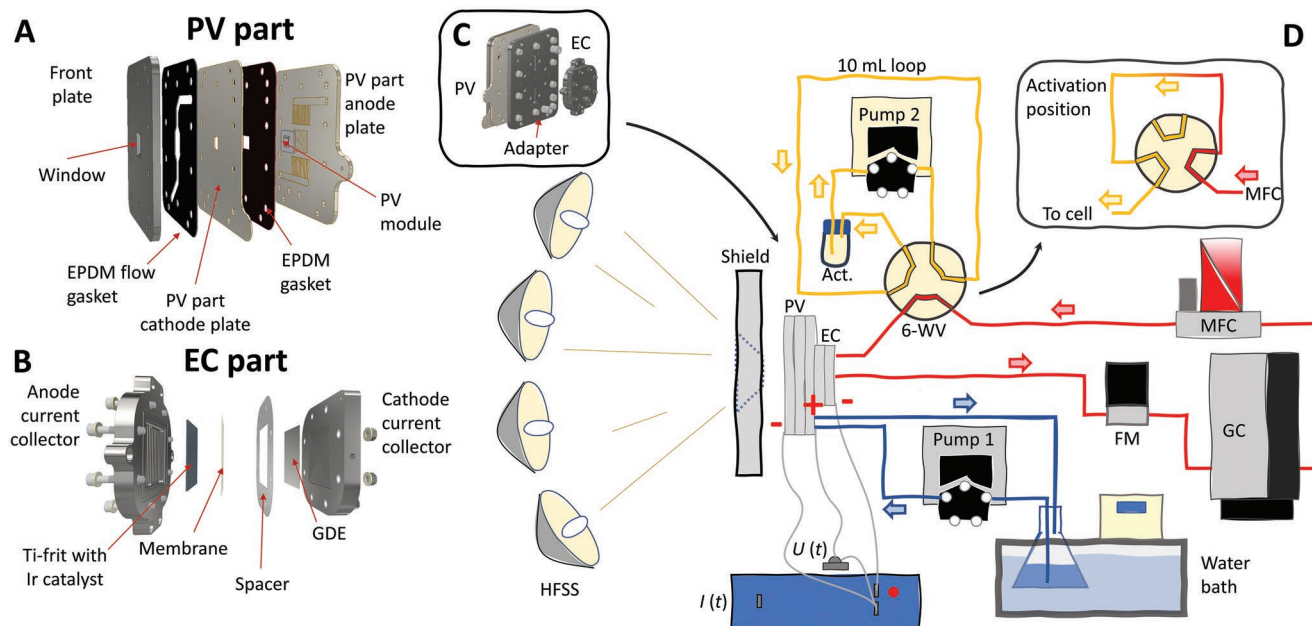

Figure 3. Representation of the custom-made P-EC cell and of the experimental organization. A) Exploded view of the PV part. B) Exploded view of the EC part. C) Assembled P-EC cell via adapter. D) Overall experimental organization. Pump 1: primary pump. Pump 2: secondary pump. $I(t)$: Booster potentiostat measuring the current. $U(t)$: Potentiostat measuring the voltage. FM: Flow-meter. GC: Gas chromatography. MFC: Mass Flow controller. 6-WV: 6-way valve. Act.: Activation liquid (1 M CsOH solution in 1:3 isopropanol/water mixture) beaker. HFSS: High Flux Solar Simulator. Blue stream: ultrapure water. Red stream: CO_2. Yellow stream: activation liquid.
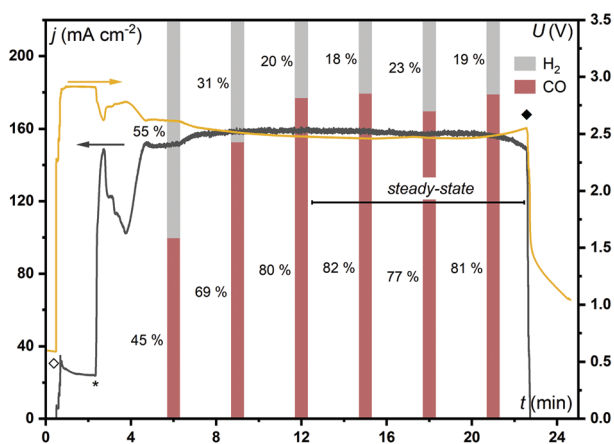
Figure 4. j, U and product selectivity for a typical short term experiment at 341 suns with the integrated P-EC cell. S_{CPV}: 0.92 cm^2. Q_{CO_2}: 312 sccm. ◇ symbol: lamps switch on. ◆ symbol: lamp switch off. * symbol: activation with 10 cm^3 of 1 M CsOH solution in 1:3 isopropanol/water mixture. Averaged T_{water}: 55 °C.

the P-EC cell. During operation, the cell is placed at a known distance from the focal plane of the 18 Xenon lamps that determines the solar concentration (see Discussion S1 (Supporting Information) for spectral characteristics and definition of concentration) thanks to a calibration made before the campaign (calibration details in Experimental section and in dedicated bibliography).[56] The flow diagram of the HFSS setup is pictured in Figure 3D and detailed in Experimental section.

Figure 4 represents characteristics of a typical integrated experiment realized with the P-EC cell irradiated with 341 suns concentrated solar irradiation. Upon switching on the lamps, the voltage and current surge to a value of 2.9 V and 750 mA (30 mA cm$^{-2}_{EC}$) respectively. At this point, the performance is limited by the electrolyzer cell. After 3 min, the 6-way valve is actuated to push the activation liquid inside the cell and produce the expected current increase of up to 4 A after an equilibration time of 3 min. The proximity of the operating

point from the maximum power point of the CPV is confirmed by the strong coupling effect between I and U traces, as any current decrease induces a sensible voltage increase and vice versa. When the current stabilizes after the equilibration time, the first GC measurement is taken and repeated every 3 min (189 sec. exactly). The gas analysis shows an initial current that is promoting equal H$_2$ and CO production. CO production then takes over and reaches a steady-state Faradaic efficiency value of ≈80% after ≈6 min. Because of the liquid trap placed downstream of the cell to avoid the injection liquid to enter the flow meter (FM) and the GC, there is a 200 mL volume on the line that buffers the gas composition change over time. This causes the delay between the moment I and U reaches steady state and the moment selectivity does. After ≈20 min of experiment, the lamps are switched off. All other experiments reported hereafter are showing similar profiles (Figures S3–S9, Supporting Information). Lengths of short-term experiments varies from 18 to 30 min. Due to the presence of a steady state regime after the equilibration time and until the lamps are turned off, the length of the experiment has no effect on the reported data since they are averaged on the steady state plateau. Continuous measurements are averaged over the 10 min that precedes lamps switch off, except for long term experiments where time resolved data are preserved. For the GC data, the 3 measurements preceding lamps switch off are considered and averaged. In all experiment, the flow at the outlet was also measured and corrected with the exact gas composition given by the GC. A complete carbon mass balance was then established considering CO$_2$ passing by the cathode, CO$_2$ converted into CO, and CO$_2$ crossing over through the membrane after conversion into CO$_3^{2-}$. This mass balance was consistent with carbonate crossing over through the membrane as the main charge carrier as discussed in Discussion S3 (Supporting Information).

The effect of solar concentration on the P-EC cell performance is summarized in **Figure 5**A. From 132 to 289 suns with the water stream temperature kept low, current and selectivity are following the sun concentration, resulting in increased solar-to-CO conversion efficiencies and single pass
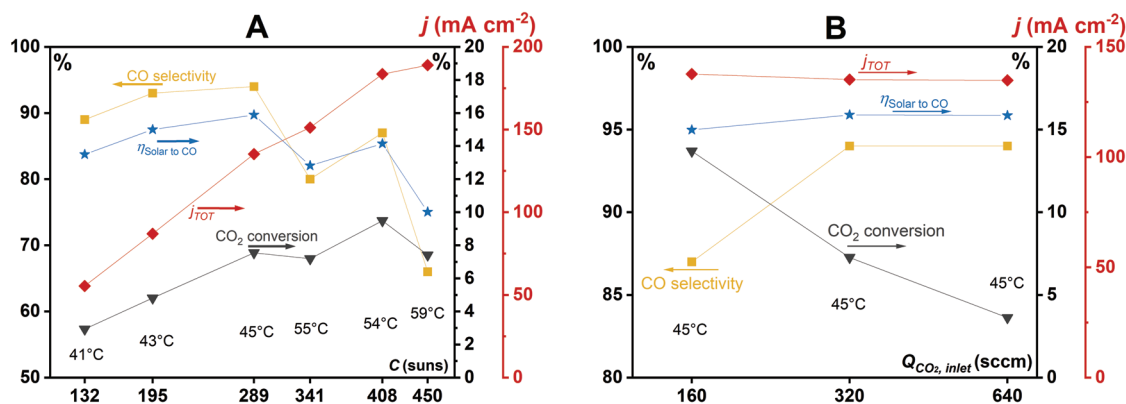

Figure 5. Current density, CO selectivity, solar-to-CO conversion efficiency, and single pass CO$_2$ conversion values, during short-term (≈20 min) experiments with the integrated P-EC cell. A) At various concentrations while Q_{CO_2} = 312 sccm. Averaged water temperature (averaged between inlet and outlet over the steady state period) is also displayed. B) At various Q_{CO_2} values while C = 289 suns. All data are reported for steady-state currents reached after a single activation with 10 cm^3 of 1 M CsOH solution in 1:3 isopropanol/water mixture: continuous data are averaged over the 10 min before lamps are switched off; GC data are averaged over the three last measurements. S_{CPV}: 0.92 cm^2. Current densities are reported for the 25 cm^2 EC surface. Lines connecting the points are only guides for the eyes.

CO_2 conversion values. At higher concentration, currents keep increasing with solar concentration and so does temperature and ohmic drop. Higher concentration, higher temperature, and ohmic drop have contradictory effects on CPV voltage but in our conditions the concentration effect was dominating and U was increasing with concentration, as can be seen in Table S2 (Supporting Information) where U of operation raises from 2.33 to 2.58 V when the concentration is increased from 132 to 450 suns. As an effect of temperature increase, CO selectivity decreases and so does solar-to-CO conversion efficiency. The decay in selectivity with temperature is consistent with what has been observed in the dark with an CsOH anolyte,[52] or with ultrapure water at the anode like in our experimental conditions (Figure S10, Supporting Information). This effect might partially be due to increased water crossover through the membrane at higher temperatures, as the water uptake of PiperIon membranes increases with temperature.[57] This faster crossover would in turn favor H_2 production. Nevertheless there might be other parameters controlling selectivity evolution with temperature as similar trends had also been observed in H-cell configurations.[58] In this set of experiments, the optimal solar-to-CO efficiency was reached at 289 suns where it is 15.8% while maintaining a j_{CO} of 136 mA cm^{-2}.

To investigate the effect of the CO_2 flow rate (Q_{CO2}), we repeated experiments at 289 suns with half and two times the 320 sccm initial CO_2 flow rate (160 and 640 sccm respectively, see Figure 5B). The CO_2 flow rate has no effect on the total current density in the EC part, which consistently equals to 136 ± 1 mA cm^{-2} in all 3 experiments. This absence of an effect on current in this range of flow is consistent with observations for dark electrolysis.[52,53] On the contrary, CO selectivity was improved by higher CO_2 flow rate when increasing from 160 to 320 sccm and went from 87 to 94% due to higher substrate availability. A further increase of the flow rate had no effect on selectivity, which plateaued at 94%. The effect of CO_2 flow rate on the CO_2 single pass conversion was almost linear and decreased from 13.6 to 3.6% as the flow increased from 160 to 640 sccm. When the CO_2 inlet flow is decreased from 320 to 160 sccm, the CO proportion at the cathode outlet increases from 12.2 to 23.63% (almost doubles), which is beneficial in terms of downstream purification. But because of poorer selectivity, the H_2 proportion increase from 0.86 to 3.37%, an increase of almost 4 times. Lowering the CO_2 flow further would provoke a higher increase in H_2 proportion and would still constitute a challenge regarding downstream purification of CO gas.

In such an EC cell, the membrane conductivity has been shown to be associated with carbonate (CO_3^{2-}) transport through the AEM resulting in CO_2 gas evolution in the anode compartment at a CO_2:O_2 ratio of 2:1. To confirm this behavior, we calculated the total carbon balance assuming a CO_3^{2-} based membrane conductivity and obtained carbon flow at the outlets ($CO_{cathode\ outlet}$ + $CO_{2\ cathode\ outlet}$ + $CO_{2\ anode\ outlet}$) equals to the carbon flow at inlet ($CO_{2\ cathode\ inlet}$) with an error below 1.2% (see Discussion S3, Supporting Information).

To probe the stability of our system, we ran an integrated experiment at 289 suns for 2.5 h (**Figure 6**). The temperature of the cooling bath for the ultrapure water recycle loop was set to 15 °C to avoid overheating over the time of the experiment.
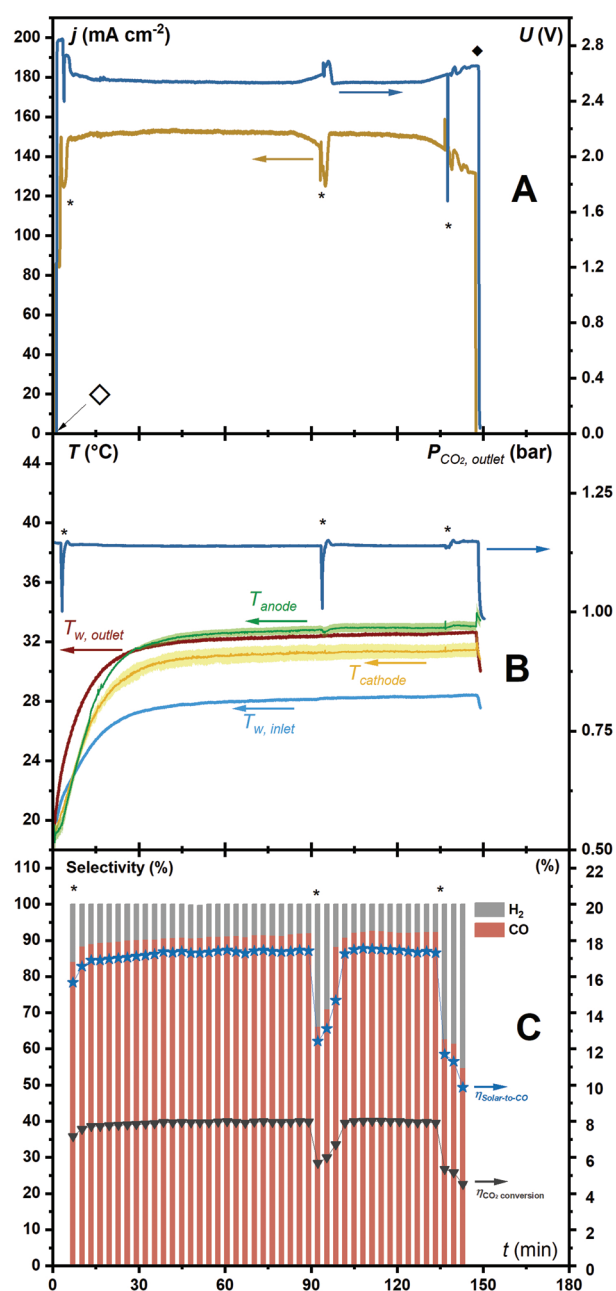

Figure 6. Summary of all recorded data during a long-term experiment performed with the integrated P-EC cell at 289 suns. S_{CPV}: 0.92 cm^2. Q_{CO2}: 320 sccm. A) U and j electrochemical traces recorded over time. B) Temperature and pressure traces recorded over time. Anode and cathode temperatures are measured at two locations each and averaged. The shaded green and yellow parts represent the deviation from average. C) CO selectivity, solar-to-CO efficiency, and CO_2 conversion efficiency over time. ◇ symbol: lamps switch on. ◆ symbol: lamps switch off. * symbol: activation with 10 cm^3 of 1 M CsOH solution in 1:3 isopropanol/water mixture.

I and U were stable for 1.5 h after which a second activation was required to recover the steady state values (Figure 6A). In this case the current density was slightly higher than for the short term experiments (+12%) due to a closer positioning of the shield that can shadow part of the incoming light arriving

from a tilted angle (more details on incoming power variation in Discussions S4 and S5, Supporting Information). The CO_2 stream outlet pressure is stable at ≈1.14 bar except upon injection where the pressure drops to 1 bar for a few seconds (Figure 6B), while the activation liquid is being pushed through the cell by the CO_2 stream. The third injection resulted in no liquid injected due to failure of the secondary pump and is the cause for the experiment's stop. The temperature of the ultrapure water stream increased over the first minutes and stabilized at 27 and 32 °C for inlet and outlet respectively. Cathode and anode temperatures were measured at two locations each and averaged, plateauing at 29 and 31 °C respectively. Selectivity was stable except during the equilibration time after injections. The average selectivity was 87%, reaching up to 92.5% at steady state (Figure 6C). The resulting solar-to-CO reaches >17% at the steady state plateau and even 17.5% at its peak values (Figure 6C). If considering the residual production of H_2, solar-to-fuel efficiency reaches up to 19%. Overall, the maximum experiment time on a single device without significant loss in performance is 2.5 h in continuous mode and >5 h under intermittent irradiation (cumulative length of all experiments undergone by a single device). After this cumulative time of experiment, we performed a Scanning electron microscopy–energy-dispersive X-ray analysis (SEM-EDX) in the cross section of the GDE (Figure S11, Supporting Information). The mapping revealed that the electrode after operation was showing the same feature as previously analyzed after dark electrolysis at 60 °C.[53] Namely the Ag layer was well maintained and the Cs^+ cations, although homogeneously present, were not forming local precipitate that could block the channels.

2. Discussion

The approach presented in this study allowed to reach solar-to-CO conversion efficiencies as high as 17%, despite the high power density in both, the CPV and EC parts, making the approach appealing from a scale up perspective. However, there is still room for improvement, especially given the efficiencies reported for lower power inputs.[4,19] To investigate and quantify the potential for improvement, the solar-to-CO efficiency is broken down into the four elemental terms from Equation 2a and presented in Table S3 (Supporting Information). In **Table 1**, the averaged values are reported for the various experiments in this study and are compared with the optimal or theoretical

values from literature.[46,59,60] In terms of potential for improvements (defined as 100 $(\eta_{i,state\text{-}of\text{-}the\text{-}art}-\eta_i)/\eta_i$), the $\eta_{P\text{-}EC,U}$ term shows the largest improvement margin. The $\eta_{P\text{-}EC,U}$ reported for solid oxide electrolysis or molten carbonate electrolysis operating at high temperature, where thermodynamics and kinetics are more favorable, are typically higher.[60] This points to a possible strategy to operate at elevated temperatures, requiring also heat supply. These requirements could potentially benefit from and be integrated in the concentrated light approach presented here. However, any temperature increase would induce a loss in the second largest potential improvement term, i.e., η_{PV}. The efficiency of the PV presented in this study is already limited by the warm operating temperature and optical losses from quartz glass window and the thin water layer used for heat management. Consequently, a significant potential for performance improvements lies in the dedicated and tailored heat management.

It is important to recall that perspectives of industrialization for such devices not only rely on high solar-to-fuel efficiency, although it is indispensable to reach low operating cost. Ultimately the plant efficiency is the metric that will drive operating cost, which requires consideration of upstream and downstream steps with all the auxiliary equipment. The plant's techno-economic relations could be assessed in dedicated techno-economic studies in which other innovations can help to decrease costs, including the cooling of the product streams that could be achieved by natural water reservoirs (river, lake or sea) rather than electricity powered equipment. Capital costs of the plant will also be important. In this case, the higher cost of CPV cell will be offset by their significantly reduced surface (equal to the solar concentration factor), resulting in beneficial economics.[50] The performance of the EC part under non-heated (thermally nonintegrated) conditions could also become important in an industrialization perspective as it could provide information on a possible grid-supported operation of the P-EC cell (in non-heated mode) when solar irradiation is not present (due to cloud or night). Such a hybrid solar-only and grid-supported operation could increase the capacity factor. Hopefully, the present article will encourage and foster techno-economic investigations in these directions.[61]

3. Conclusions

In this study, we have demonstrated the feasibility of P-EC CO_2–to-CO conversion under highly concentrated light irradiation (up to 450 suns). Thanks to the utilization of concentrated irradiation, a high power density device was obtained, with CO current density in the CPV and EC above 4 and 0.15 A cm^{-2}, respectively. Appropriate choices of material and method (zero-gap, alkaline activation, and thermal management) allowed to keep activation overpotentials and ohmic losses minimal, resulting in solar-to-CO and solar-to-fuel conversion efficiencies as high as 17% and 19%, respectively. Combination of high power input and high solar-to-CO conversion efficiency resulted in this first P-EC demonstration with production rates above 1 L_{CO} h^{-1}. This study shows that high concentrated light P-EC cells are promising devices for resource efficient CO_2 valorization at high power input and pave a path toward more economic solar fuel production.

Table 1. Averaged value reported in this study for four elemental efficiencies compared with state of the art reports and the corresponding potential for improvement.

	η_{PV} [%]	η_{op} [%]	$\eta_{EC,I}$ [%]	$\eta_{P\text{-}EC,U}$ [%]
This study (average)	33.28	92.66	85.52	53.49
State of the art	47.10[46]	100.00[a]	100.00[59]	92.00[60]
Potential for improvement	41	8	17	72

[a] Theoretical value

**ADVANCED
SCIENCE NEWS**

www.advancedsciencenews.com

**ADVANCED
ENERGY
MATERIALS**

www.advenergymat.de

4. Experimental Section

CPV Module Preparation: The steps of its fabrication are pictured in Figure S12 (Supporting Information). The CPV module was assembled on a 290×390 mm^2 copper plate that had a 10×10.5 mm^2 stage at its center to hold the CPV cell. This copper plate was dipped in 1% H_2SO_4 solution for 1 h before module preparation to remove the natural oxide layer and subsequently washed with acetone followed by isopropanol (IPA) sonication bath. The 1 cm^2 photoactive area CPV cell used was a III–V material-based triple-junction GaInP/GaInAs/Ge solar cells from Azur space (3C 44 type version MC/Glass). These cells had a Ag/Au alloy back contact that was soldered into the copper stage with a Sn-96/Ag-4 (wt.%) solder. A 2 mm long solder wire was mechanically pressed into a thin pad and inserted between the stage and the CPV, and put into a N$_2$ saturated oven at 230 °C for 1 min to realize the soldering without favoring copper oxide layer formation. A PTFE frame was glued around the CPV with high thermal resistance epoxy (Loctite EA 9497) to isolate electrically the cathodic collector from the copper plate potential. The epoxy was cured at 80 °C for 90 min in an open air oven. A 0.25 mm thick aluminum foil was cut into 1×3 cm^2 rectangle and cut at appropriate location to create a passage for screws when finally connected with PV part cathode plate (see later). These rectangles were bent to take the shape of the PTFE frame. Thin layers of Cr (5 nm) and Au (150 nm) are sputtered on these Al rectangles to facilitate the subsequent wire bonding (see later). The aluminum rectangle foils were then glued to the PTFE frame with the same high thermal resistance epoxy described above. The two gold-coated edges of the solar cell front are connected to the Au coated Al rectangle foil, via gold wire bonding (diameter: 25 μm). 60 bonds were arranged on each side stripe of the CPV. The wire bonds were then protected by applying a black protective epoxy (EPO-TEK H740E-2) on top of it, resulting in a slight decrease of active CPV surface to 0.92 cm^2 (Figure S13, Supporting Information). The mechanical and electrical connections of this module with the PV part anode plate was made by 10 M1 stainless steel microscrews. The electrical contact between the CPV module negative side and the PV part cathode plate was made by squeezing the Al foils between the cathode plate and 0.9 mm stainless steel threaded wedged, with 2×3 M1.6 stainless steel microscrews.

PV Part Assembly: The PV part of the integrated P-EC cell used for the integrated measurements under solar irradiation was made from different metal plates stacked together. The PV to EC adapter plate described below was used as the bottom squeezing plate. It contains the inlet and outlet for the water channels and also channels connecting this water stream from PV part to EC and back to PV part. On top of it, the PV part anode plate, made of titanium (grade 2), receives the copper-based CPV module (described above) fixed with 10 M1 threads placed at the module expected position to form a mechanical and electrical contact. A 1/32″ thick EPDM gasket with a 18×22 mm opening for the CPV stage was put on top of the anode + CPV module assembly and the aluminum rectangle foils were put on top of it in order to isolate electrically the components connecting the PV anodic and cathodic parts. The threaded stainless still wedges were put under the Al rectangle foils and the PV part cathode plate (Ti grade 2) was put on top of the stack. Using M1.6 stainless steel microscrews, the stainless steel wedges were compressed against the PV part cathode plate, squeezing the Al foils against it. Another 1/32″ thick EPDM sheet was placed on top of the stack with a specific water flow channel to guide the stream of ultrapure water on top of the CPV. The stack was closed with a stainless steel plate (standard 304) used as front plate in which a window is designed with a 45° angle to allow for the irradiation of the concentrated light arriving from lamps arranged with a rim angle of 45°. A 2 mm thick space was made in this plate to fit the quartz glass window that was glued with high thermal resistance epoxy (Loctite EA 9497) prior to closing the cell. Compression of the PV part was achieved between the adapter plate and front plate through a pattern of 10 M8 screws that are isolated with cable shrink and gradually tighten to 7 nm. The PV to EC adapter was thus connected to the EC stack with a set of 6x M5 stainless steel screws to create a mechanical and electrical contact and connect the water channels for both parts.

Electrode Preparation: A dispersion of silver nanoparticles ($d_{avg} < 100$ nm, Sigma-Aldrich) was prepared in a 1:1 isopropanol/water mixture (25 mg cm^{-3}), together with 20 wt.% Sustainion XC-2 ionomer. As for the anode catalyst, IrO$_x$ nanoparticles (Fuel-Cell Store) were dispersed in an identical solvent mixture and ionomer concentration, but with a IrO$_x$ concentration of 20 mg cm^{-3} and a Sustainion XB-7 type ionomer. The IrO$_x$ dispersion was homogenized in an ultrasonic bath for 20 min (keeping the bath temperature below 35 °C), while a high-power immersion sonotrode was used to disperse the Ag nanoparticles. The Ag dispersion was spray-coated on Sigracet 39BB carbon GDLs preheated on a hotplate at 100 °C, with a hand-held airbrush and compressed air carrier gas (≈ 100 cm^3 min^{-1}). The anode catalyst was spray-coated similarly, on a 1 mm thick, porous titanium frit. The cathode catalyst loading was 2.7 ± 0.1 mg cm^{-2} and the anode catalyst amount was 1.0 ± 0.1 mg cm^{-2}. A commercially available anion exchange membrane (AEM) was used to separate the anode and the cathode chambers, namely PTFE-reinforced 15-μm thick PiperION TP-85 from Versogen LLC. The membranes were activated (ion-exchanged) before use for 24 h in 1 M CsOH solution, which was exchanged to a fresh solution after the first 5 h.

EC Part Assembly: Similarly to our previous studies,[52,62] the zero-gap electrolyzer cell consists of an anode current collector (with a anolyte flow pattern), the porous Ti frit with IrO$_x$ catalyst layer on its side in direct contact with the AEM, the gas-diffusion electrode (GDE) with the Ag catalyst layer facing the AEM, a spacer element to set the compression ratio of the GDE, and a cathode current collector with a rectangular shape concentric flow pattern with a central CO$_2$ gas inlet, and the product outlet was on the perimeter of the flow pattern. 8 M5 bolt screws were used to assemble the electrolyzer cell, gradually applying a torque of 3 nm. The active surface was rectangular with side length of 5 cm, resulting in a geometrical surface of area, $S_{EC} = 25$ cm^2. Except otherwise noted explicitly, the current densities reported in the manuscript were normalized to the EC active surface and not CPV surface. Both, cathode and anode plates, had two dedicated slots to fit thermal probes near the electrodes.

Integrated Device Through PV to EC Adapter: The adapter element also provides the electrical connection between the two compartments and manages the stream of water to the anode side of the electrolyzer. This solution uses two separate screw sets: one to tighten the illuminated PV holder part and another screw set to assemble the CO$_2$ electrolyzer cell, enabling homogeneous compression in both components.

Thermal Shield: Because the experimental strategy to control the solar irradiation in the CPV (in terms of power and homogeneity) is to move it away from the lamps focal plan, a significant portion of the light was irradiating the side of the CPV target. To avoid excessive heating or thermal artefacts, a 3 cm thick aluminum thermal shield was put in front of the cell, with a 45° angle 33×33 mm^2 window (see Figure S14 (Supporting Information) for a picture). The shield is drilled with 12 perpendicular 8 mm-diameter channels that were connected together externally and flushed with tap water during the experiment to maintain its temperature near room temperature. Its surface is covered with white thermal paint to avoid light reflection. Despite its 45° angle window, a small distance between the shield and the cell slightly affects the overall light intensity reaching the cell as discussed in Discussion S5 (Supporting Information).

HFSS and Calibration: EPFL's High Flux Solar Simulator (HFSS) facility consists of 18 Xenon arc lamps, each with 2.5 kW$_{el}$ power, each positioned inside a partial ellipse reflector. The calibration of the HFSS was done by an established process using a Lambertian target and a CCD camera (Basler scA 1400–17 gm, 1.5 MP, 12 bit pixel depth) to obtain the grayscale image.[56] Calibration was done for different positions away from the focal plane and for different lamp currents to achieve uniform flux profiles on the target area of 1 cm^2 and various irradiation concentrations. Characterization of CPV and integrated experiments were performed using all lamps in the outer ring (12 lamps) at concentrations between 132 and 450. To be noted that the spectrum of a Xe-arc lamp normalized to 1 kW m^{-2} is different from AM1.5G spectrum and result in less current as detailed in Discussion S1 (Supporting Information).

CPV Characterization: I–U curves of the CPV module measured under simulated 1 sun irradiation where performed with a lab scale solar simulator (OAI's TRI-SOL solar simulator 1–1.6 KW, see Discussion S1 (Supporting Information) for more information on spectrum) and recorded using a Biologic VSP-300 potentiostat driven by EC lab software. I–U curves of the CPV module at higher concentration where recorded in the assembled and water cooled PV part in HFSS using a Biologic HCP803 potentiostat with (up to 80 A) booster option and by connecting the PV part anode and cathode directly in a two electrode setup.

Dark Electrochemical Characterization: The dark electrochemical measurements were performed using a Biologic VMP-300 type potentiostat/galvanostat instrument, equipped with electrochemical impedance spectroscopy (EIS) and high current booster options (up to 10 A). All the dark experiments (including the EIS measurements) were performed using the potentiostat with the booster connected. The measurements were conducted in a two-electrode setup, and the total cell voltage was given as the voltage difference between the anode and the cathode. EIS spectra had been taken at constant cell voltage with added 10 mV RMS perturbation in the frequency range 100 kHz down to 0.1 Hz, with 10 points per frequency decade. To help in distinguishing spectra they are shifted along the ordinate in Figure S2D.

Integrated Experiments: The integrated experimental setup is pictured in Figure 3. The thermal shield cooled with tap water was put in the front of the P-EC cell to protect the setup and avoid overestimation of heat management effect by blocking any stray radiation. Once in place, a high current potentiostat (Biologic HCP803 potentiostat with up to 80 A booster option) was connected between the PV part cathode plate and the cathodic EC plate and run in chronoamperometry mode at 0 V applied potential to record the current. Additionally, a Palmsens (Emstat 3+) potentiostat was connected between the anodic and cathodic PV plates and set to open circuit potential measurement mode to record the voltage. The water line was connected to the adapter to supply the ultrapure stream that is coming from a temperature controlled beaker and circulated with a primary pump at a flow (Q_{water}) varying between 1 to 4 L min^{-1}. This water flow rate was necessary to avoid risk of CPV cell overheating (see Discussion S6 (Supporting Information) for discussion on water management). The CO_2 line was supplied at a constant flow, controlled by a Mass Flow Controller (MFC, F-201CV from Bronkhorst) and was passed through a 6-way valve that was operating the injection, the activation liquid that was inside a 10 mL activation loop when switched (inset in Figure 3D) and refilled thanks to a secondary pump and an activation liquid beaker. The cathodic stream was then entered the EC cathode and reacted upon passage by the GDE. The outcoming CO_2, CO, and H_2 stream flow and pressure were measured by a flowmeter (FM, M-500 sccm-D from Alicat) and then analyzed by an online gas chromatography (GC, see below). To be noted that due to the high power of the 45 kW HFSS source, access to the cell and setup during operation was not possible and all devices must be operated from a separated control room and all gas cylinder (CO_2 supply, compressed air for 6-way valve actuation or Ar and He for GC columns) were connected from outside of the room.

MFC and FM Calibration: MFC and FM were calibrated for various CO_2 flow rate with a Standard Air Flow Calibrator (Gilian Gilibrator-2 NIOSH) to provide a linear correction factor between instrument flow and real flow ($R^2 = 1$ in both cases).

Gas Analysis: The composition of the cathode outlet gas composition was analyzed with an online gas chromatography instrument (490 μ-GC, Agilent technologies) every 189 s during integrated experiments. The μ-GC was calibrated by sampling gas mixture of three known concentrations (100, 1000, and 10 000 ppm for H_2 and CO_2; 1%, 3%, and 9% for CO).

Solar-to-CO and Solar-to-Fuel Conversion Efficiencies Determination: The solar-to-CO conversion efficiency is calculated as described in Equation 2a. The solar-to-fuel efficiency is calculated by adding the solar-to-H_2 efficiency calculated by the same equation but where I_{CO} is replace by I_{H2} and $E^0_{O_2/H_2O} - E^0_{CO_2/CO} = 1.33\,\text{V}$ is replaced by $E^0_{O_2/H_2O} - E^0_{H^+/H_2} = 1.23\,\text{V}$.

Conversion Efficiency Determination: During integrated experiments, the flow of CO_2 entering the cell was controlled with a MFC, allowing for the knowledge of the inlet amount, while the partial current for CO reflects the converted amount. It is thus possible to estimate the CO_2 single pass conversion efficiency with Equation 3:

$$\eta_{CO_2\text{ conversion}} = \frac{\dfrac{I_{CO}}{2F}}{\dfrac{Q_{CO_2}d_{CO_2}}{M_{CO_2}}} \tag{3}$$

Where Q_{CO_2} is the CO_2 volume flow rate entering the cell, d_{CO_2} is CO_2 density, and M_{CO_2} is the molar weight of CO_2.

Supporting Information

Supporting Information is available from the Wiley Online Library or from the author.

Acknowledgements

Conflict of Interest

The authors declare no conflict of interest.

Data Availability Statement

The data that support the findings of this study are available from the corresponding author upon reasonable request.

Keywords

[1] S. Giménez, J. Bisquert, *Photoelectrochemical Solar Fuel Production: From Basic Principles to Advanced Devices*, Springer, S.L, **2016**.

[2] P. De Luna, C. Hahn, D. Higgins, S. A. Jaffer, T. F. Jaramillo, E. H. Sargent, *Science* **2019**, *364*, eaav3506.

**ADVANCED
SCIENCE NEWS**

www.advancedsciencenews.com

**ADVANCED
ENERGY
MATERIALS**

www.advenergymat.de

[3] C. E. Creissen, M. Fontecave, *Adv. Energy Mater.* **2021**, *11*, 2002652.

[4] Y. Xiao, Y. Qian, A. Chen, T. Qin, F. Zhang, H. Tang, Z. Qiu, B.-L. Lin, *J. Mater. Chem. A* **2020**, *8*, 18310.

[5] C. R. Cox, M. T. Winkler, J. J. H. Pijpers, T. Buonassisi, D. G. Nocera, *Energy Environ. Sci.* **2013**, *6*, 532.

[6] L. Pan, J. H. Kim, M. T. Mayer, M.-K. Son, A. Ummadisingu, J. S. Lee, A. Hagfeldt, J. Luo, M. Grätzel, *Nat. Catal.* **2018**, *1*, 412.

[7] P. B. Pati, R. Wang, E. Boutin, S. Diring, S. Jobic, N. Barreau, F. Odobel, M. Robert, *Nat. Commun.* **2020**, *11*, 3499.

[8] Y. Sugano, A. Ono, R. Kitagawa, J. Tamura, M. Yamagiwa, Y. Kudo, E. Tsutsumi, S. Mikoshiba, *RSC Adv.* **2015**, *5*, 54246.

[9] M. Schreier, L. Curvat, F. Giordano, L. Steier, A. Abate, S. M. Zakeeruddin, J. Luo, M. T. Mayer, M. Grätzel, *Nat. Commun.* **2015**, *6*, 7326.

[10] N. C. Deb Nath, S. Y. Choi, H. W. Jeong, J.-J. Lee, H. Park, *Nano Energy* **2016**, *25*, 51.

[11] M. Schreier, F. Héroguel, L. Steier, S. Ahmad, J. S. Luterbacher, M. T. Mayer, J. Luo, M. Grätzel, *Nat. Energy* **2017**, *2*, 17087.

[12] W. Deng, L. Zhang, H. Dong, X. Chang, T. Wang, J. Gong, *Chem. Sci.* **2018**, *9*, 6599.

[13] T. Arai, S. Sato, K. Sekizawa, T. M. Suzuki, T. Morikawa, *Chem. Commun.* **2019**, *55*, 237.

[14] L. Q. Zhou, C. Ling, H. Zhou, X. Wang, J. Liao, G. K. Reddy, L. Deng, T. C. Peck, R. Zhang, M. S. Whittingham, C. Wang, C.-W. Chu, Y. Yao, H. Jia, *Nat. Commun.* **2019**, *10*, 4081.

[15] Y. Mi, Y. Qiu, Y. Liu, X. Peng, M. Hu, S. Zhao, H. Cao, L. Zhuo, H. Li, J. Ren, X. Liu, J. Luo, *Adv. Funct. Mater.* **2020**, *30*, 2003438.

[16] S. Esiner, J. Wang, R. A. J. Janssen, *Cell Reports Physical Science* **2020**, *1*, 100058.

[17] M. Asadi, M. H. Motevaselian, A. Moradzadeh, L. Majidi, M. Esmaeilrad, T. V. Sun, C. Liu, R. Bose, P. Abbasi, P. Zapol, A. P. Khodadoust, L. A. Curtiss, N. R. Aluru, A. Salehi-Khojin, *Adv. Energy Mater.* **2019**, *9*, 1803536.

[18] A. Sacco, R. Speranza, U. Savino, J. Zeng, M. A. Farkhondehfal, A. Lamberti, A. Chiodoni, C. F. Pirri, *ACS Sustainable Chem. Eng.* **2020**, *8*, 7563.

[19] W.-H. Cheng, M. H. Richter, I. Sullivan, D. M. Larson, C. Xiang, B. S. Brunschwig, H. A. Atwater, *ACS Energy Lett.* **2020**, *5*, 470.

[20] K. Jiang, S. Siahrostami, A. J. Akey, Y. Li, Z. Lu, J. Lattimer, Y. Hu, C. Stokes, M. Gangishetty, G. Chen, Y. Zhou, W. Hill, W.-B. Cai, D. Bell, K. Chan, J. K. Nørskov, Y. Cui, H. Wang, *Chem* **2017**, *3*, 950.

[21] F. Urbain, P. Tang, N. M. Carretero, T. Andreu, L. G. Gerling, C. Voz, J. Arbiol, J. R. Morante, *Energy Environ. Sci.* **2017**, *10*, 2256.

[22] T. Haas, R. Krause, R. Weber, M. Demler, G. Schmid, *Nat. Catal.* **2018**, *1*, 32.

[23] S. Y. Chae, S. Y. Lee, S. G. Han, H. Kim, J. Ko, S. Park, O.-S. Joo, D. Kim, Y. Kang, U. Lee, Y. J. Hwang, B. K. Min, *Sustainable Energy Fuels* **2020**, *4*, 199.

[24] B. Kim, H. Seong, J. T. Song, K. Kwak, H. Song, Y. C. Tan, G. Park, D. Lee, J. Oh, *ACS Energy Lett.* **2020**, *5*, 749.

[25] H. S. Jeon, J. H. Koh, S. J. Park, M. S. Jee, D.-H. Ko, Y. J. Hwang, B. K. Min, *J. Mater. Chem. A* **2015**, *3*, 5835.

[26] V. Andrei, B. Reuillard, E. Reisner, *Nat. Mater.* **2020**, *19*, 189.

[27] T. A. Kistler, M. Y. Um, J. K. Cooper, I. D. Sharp, P. Agbo, *Adv. Energy Mater.* **2021**, *11*, 2100070.

[28] G. M. Sriramagiri, N. Ahmed, W. Luc, K. D. Dobson, S. S. Hegedus, F. Jiao, *ACS Sustainable Chem. Eng.* **2017**, *5*, 10959.

[29] W. H. Lee, C. Lim, E. Ban, S. Bae, J. Ko, H.-S. Lee, B. K. Min, K.-Y. Lee, J. S. Yu, H.-S. Oh, *Appl. Catal., B* **2021**, *297*, 120427.

[30] T. Arai, S. Sato, T. Kajino, T. Morikawa, *Energy Environ. Sci.* **2013**, *6*, 1274.

[31] T. Arai, S. Sato, T. Morikawa, *Energy Environ. Sci.* **2015**, *8*, 1998.

[32] U. Kang, S. K. Choi, D. J. Ham, S. M. Ji, W. Choi, D. S. Han, A. Abdel-Wahab, H. Park, *Energy Environ. Sci.* **2015**, *8*, 2638.

[33] X. Zhou, R. Liu, K. Sun, Y. Chen, E. Verlage, S. A. Francis, N. S. Lewis, C. Xiang, *ACS Energy Lett.* **2016**, *1*, 764.

[34] U. Kang, H. Park, *J. Mater. Chem. A* **2017**, *5*, 2123.

[35] H. Yang, N. Han, J. Deng, J. Wu, Y. Wang, Y. Hu, P. Ding, Y. Li, Y. Li, J. Lu, *Adv. Energy Mater.* **2018**, *8*, 1801536.

[36] J. L. White, J. T. Herb, J. J. Kaczur, P. W. Majsztrik, A. B. Bocarsly, *J. CO2 Util.* **2014**, *7*, 1.

[37] G. Piao, S. H. Yoon, D. S. Han, H. Park, *ChemSusChem* **2020**, *13*, 698.

[38] T. Sekimoto, H. Hashiba, S. Shinagawa, Y. Uetake, M. Deguchi, S. Yotsuhashi, K. Ohkawa, *J. Phys. Chem. C* **2016**, *120*, 13970.

[39] Gurudayal, J. Bullock, D. F. Srankó, C. M. Towle, Y. Lum, M. Hettick, M. C. Scott, A. Javey, J. Ager, *Energy Environ. Sci.* **2017**, *10*, 2222.

[40] T. N. Huan, D. A. Dalla Corte, S. Lamaison, D. Karapinar, L. Lutz, N. Menguy, M. Foldyna, S.-H. Turren-Cruz, A. Hagfeldt, F. Bella, M. Fontecave, V. Mougel, *Proc. Natl. Acad. Sci. USA* **2019**, *116*, 9735.

[41] J. W. B. Gurudayal, J. Bullock, H. Wang, J. Eichhorn, C. Towle, A. Javey, F. M. Toma, N. Mathews, J. W. Ager, *Energy Environ. Sci.* **2019**, *12*, 1068.

[42] Z. Chen, T. Wang, B. Liu, D. Cheng, C. Hu, G. Zhang, W. Zhu, H. Wang, Z.-J. Zhao, J. Gong, *J. Am. Chem. Soc.* **2020**, *142*, 6878.

[43] D. Ren, N. W. X. Loo, L. Gong, B. S. Yeo, *ACS Sustainable Chem. Eng.* **2017**, *5*, 9191.

[44] A. Bagger, W. Ju, A. S. Varela, P. Strasser, J. Rossmeisl, *ChemPhysChem* **2017**, *18*, 3266.

[45] M. Green, E. Dunlop, J. Hohl-Ebinger, M. Yoshita, N. Kopidakis, X. Hao, *Prog. Photovoltaics* **2021**, *29*, 3.

[46] B. L. Smith, M. Woodhouse, K. A. W. Horowitz, T. J. Silverman, J. Zuboy, R. M. Margolis, *Photovoltaic (PV) Module Technologies: 2020 Benchmark Costs and Technology Evolution Framework Results*, National Renewable Energy Lab. (NREL), Golden, CO (United States), **2021**.

[47] S. Jin, Z. Hao, K. Zhang, Z. Yan, J. Chen, *Angew. Chem., Int. Ed.* **2021**, *60*, 20627.

[48] A. Nakamura, Y. Ota, K. Koike, Y. Hidaka, K. Nishioka, M. Sugiyama, K. Fujii, *Appl. Phys. Express* **2015**, *8*, 107101.

[49] J. Jia, L. C. Seitz, J. D. Benck, Y. Huo, Y. Chen, J. W. D. Ng, T. Bilir, J. S. Harris, T. F. Jaramillo, *Nat. Commun.* **2016**, *7*, 13237.

[50] M. Dumortier, S. Tembhurne, S. Haussener, *Energy Environ. Sci.* **2015**, *8*, 3614.

[51] J. He, C. Janáky, *ACS Energy Lett.* **2020**, *5*, 1996.

[52] B. Endrődi, E. Kecsenovity, A. Samu, T. Halmágyi, S. Rojas-Carbonell, L. Wang, Y. Yan, C. Janáky, *Energy Environ. Sci.* **2020**, *13*, 4098.

[53] B. Endrődi, A. Samu, E. Kecsenovity, T. Halmágyi, D. Sebők, C. Janáky, *Nat. Energy* **2021**, *6*, 439.

[54] S. Tembhurne, F. Nandjou, S. Haussener, *Nat. Energy* **2019**, *4*, 399.

[55] M. C. O. Monteiro, F. Dattila, B. Hagedoorn, R. García-Muelas, N. López, M. T. M. Koper, *Nat. Catal.* **2021**, *4*, 654.

[56] G. Levêque, R. Bader, W. Lipiński, S. Haussener, *Opt. Express* **2016**, *24*, A1360.

[57] J. Wang, Y. Zhao, B. P. Setzler, S. Rojas-Carbonell, C. Ben Yehuda, A. Amel, M. Page, L. Wang, K. Hu, L. Shi, S. Gottesfeld, B. Xu, Y. Yan, *Nat. Energy* **2019**, *4*, 392.

[58] R. Kostecki, J. Augustynski, *Ber. Bunsenges. Phys. Chem.* **1994**, *98*, 1510.

[59] M. Wang, L. Chen, T.-C. Lau, M. Robert, *Angew. Chem., Int. Ed.* **2018**, *57*, 7769.

[60] R. Küngas, *J. Electrochem. Soc.* **2020**, *167*, 044508.

[61] A. J. Welch, I. A. Digdaya, R. Kent, P. Ghougassian, H. A. Atwater, C. Xiang, *ACS Energy Lett.* **2021**, *6*, 1540.

[62] B. Endrődi, E. Kecsenovity, A. Samu, F. Darvas, R. V. Jones, V. Török, A. Danyi, C. Janáky, *ACS Energy Lett.* **2019**, *4*, 1770.